Available online at www.sciencedirect.com
ScienceDirect
Journal of the European Ceramic Society 30 (2010) 2289–2300
www.elsevier.com/locate/jeurceramsoc

Synthesis of carbon-rich hafnia thin films by pulsed laser deposition

Dušan A. Pejaković [a,*], Jochen Marschall [a], Mekha R. George [b], Bridget R. Rogers [b], Wesley R. Nieveen [c], Vasil Pajcini [c]

[a] *Molecular Physics Laboratory, SRI International, 333 Ravenswood Ave., Menlo Park, CA 94025, United States*
[b] *Department of Chemical Engineering, Vanderbilt University, 24th & Garland Aves., 107 Olin Hall, Nashville, TN 37235, United States*
[c] *Evans Analytical Group, 810 Kifer Rd., Sunnyvale, CA 94086, United States*

Abstract

Carbon-rich ceramics are an emerging class of materials with attractive high-temperature properties, including resistance to crystallization, dense microstructure, and low porosity. We explored direct synthesis of carbon-rich hafnia, which is known to form as a compact interlayer in the oxide scales of oxidized hafnium carbide. The material was synthesized by pulsed laser deposition, using pure HfO_2 targets in C_2H_2 background gas at low pressures. Stable films up to 700 nm thick and with high molar fractions (∼0.1–0.45) of carbon were obtained. The predominant chemical bonding of Hf and O atoms is that of oxygen-deficient HfO_2, while carbon is present in elemental or hydrogenated forms. Annealing at 600 °C leads to loss of most of the hydrogen from the films, which is accompanied by enhanced sp^2 bonding of carbon. The films have amorphous, compact, and finely grained microstructure. Carbon molar fractions higher than ∼0.2 inhibit microcrystallinity to at least 600 °C.

Keywords: Films; Transition metal oxides; Carbon; Refractories; HfO_2

1. Introduction

Incorporation of large molar fractions of carbon in a ceramic material can result in unexpected and useful high-temperature properties. Well-known examples of such materials are polymer-derived ceramics (PDCs) obtained by pyrolysis of highly cross-linked polymers.[1] The PDC systems that have been synthesized and studied to date are varieties of silicon oxycarbide (SiCO),[2] silicon carbonitride (SiCN),[3] and, most recently, silicon oxycarbonitride (SiCNO).[4,5] These systems are characterized by mostly amorphous structures and the presence of excess (or "free") carbon relative to the stoichiometric mixtures of either SiC and SiO_2 or SiC and Si_3N_4. Intuitively, the presence of zones with free carbon in a ceramic matrix should cause lower thermal stability and inferior oxidation resistance. However, it has been reported that a SiCN PDC exhibits passive oxidation behavior despite the presence of free carbon.[6,7] A recent study of carbon-rich SiCO derived from polyhydridomethylsiloxane and divinyl benzene showed that microcrystallinity and phase separation are inhibited to at least 1200 °C, while oxidation resistance in ambient air is rather high at temperatures as high as 1000 °C.[8] In addition, PDCs show excellent mechanical properties at high temperatures, including viscoelasticity and low creep. Recent molecular dynamics calculations and the accompanying NMR data suggest that carbon is aromatically bonded and may be in the form of a graphene network.[9] It has been proposed that in SiCO PDCs a unique nanostructure, consisting of SiO_2 nanodomains and a network of sp^2 carbon is responsible for the resistance to microcrystallinity, phase separation, and creep.[10] It has also been argued that such nanostructure has a negative enthalpy relative to the crystalline phases (SiC, cristobalite, and graphite), implying that crystallization is inhibited due to thermodynamic, rather than kinetic reasons.[11]

Another class of carbon-rich ceramic systems, which has been studied to a much lesser extent, comprises carbon-rich interlayer oxides formed during high-temperature oxidation of transition metal (Hf, Zr, and Ti) carbides. None of these materials have been directly synthesized prior to this work. Investigations of these systems have been reported by Bargeron et al.,[12–15] who investigated high-temperature oxidation of CVD-deposited HfC, Shimada et al.,[16–21] who studied oxidation of single crystals of HfC, ZrC, and TiC, and Wuchina and Opeka,[22] who identified a carbon-rich interlayer after both furnace oxidation and arcjet testing of HfC. For all three carbides, three distinct

* Corresponding author. Tel.: +1 650 859 5129; fax: +1 650 859 6196.
E-mail address: dusan.pejakovic@sri.com (D.A. Pejaković).

0955-2219/$ – see front matter © 2010 Elsevier Ltd. All rights reserved.
doi:10.1016/j.jeurceramsoc.2010.01.009

layers are observed in the cross-sections of oxidized samples: a layer of residual carbide, an external oxide layer with a low carbon content, and an interlayer of oxygen-deficient oxide with a high carbon content (up to 25 at%). The two-layer structure of oxide scales is completely analogous for HfC and ZrC; the case of TiC is somewhat more complicated – due to the fact that both TiO_2 and Ti_3O_5 are present in the oxide scales – and has not been investigated as thoroughly.

The contrast between the interlayer and outer oxide microstructures is striking, with the external oxide containing pores and cracks, whereas the interlayer is fine-grained, compact, and virtually pore-free. Other attractive high-temperature properties of the interlayer material, reported for the case of oxidized HfC, are high hardness and high electrical conductivity, which are both comparable to those of HfC.[14,15] A particularly intriguing feature is the sharply defined interface between the two oxide layers,[14,15] which suggests that the carbon-rich interlayer is a distinctly different phase from the low-carbon outer oxide layer,[15] despite the gradual change in the O- and C-atom concentrations and no indications of changes in chemical bonding across this interface.[19,20] Studies of oxidized ZrC have shown that the interlayer has nanocrystalline-to-amorphous structure, with c-ZrO_2 crystallite sizes in the range 2–10 nm,[17] while the outer oxide layer contains crystallites larger than 20 nm.[20] The Raman spectroscopy of the interlayer has shown the presence of elemental sp^2-bonded amorphous carbon.[17,21] The oxidation experiments and oxidation kinetics modeling[12,14,15] have indicated that the interlayer is the primary diffusion barrier for oxygen, and probably for carbon as well.[19]

The published data summarized above suggest the following explanation for the remarkable properties of carbon-rich interlayer oxides. High molar fraction of sp^2-bonded elemental carbon in the interlayer inhibits crystallization of the transition metal oxide. In turn, the amorphous structure of the interlayer inhibits propagation of pores and cracks. Finally, pore-free and compact structure enhances the diffusion barrier properties.

Bargeron et al. suggested that carbon-rich Hf oxide could be produced as a monolithic coating and find application as a protective high-temperature material.[14] Direct synthesis of carbon-rich hafnia films is also of fundamental interest, because it will allow systematic investigations of the role of free carbon in controlling the nanostructure and high-temperature properties in this system. In particular, given that it appears that free carbon inhibits long-range crystallinity in the interlayer, it is important to determine the requirements for carbon spatial distribution on the nanoscale and the limiting carbon molar fraction for this inhibition to take place. Another key question is how thermodynamically stable is the interlayer material (with respect to phase separation) and, related to this, could the well-defined boundary between the interlayer and the outer oxide layer be a signature of a true phase transition occurring upon the gradual addition/removal of carbon. Such investigations would answer questions that are relevant to PDCs as well. Keeping in mind that the major difference between the two systems is that in PDCs, in addition to free carbon, there is also stoichiometric carbon that is bonded to Si atoms, the role of free carbon in controlling the microstructure and high-temperature properties may be similar in PDCs and carbon-rich oxides.

The main challenge in synthesizing a material analogous to the interlayer carbon-rich oxides is to reproduce the specific, exceptionally finely grained nanostructure observed in these systems, with a high fraction of elemental carbon dissolved in an essentially amorphous oxide matrix. Another key issue is preserving the desired chemical bonding—that of MO_2 (M = Hf, Zr) and sp^2 carbon, without significant carbide contribution. Thus, the synthesis route must avoid the carbide formation by carbothermal reduction, which has been reported to occur at temperatures below 1500 °C.[23]

In this work, direct synthesis of carbon-rich hafnia films was performed by pulsed laser deposition (PLD). While PLD is not practical for the production of either bulk materials or protective coatings for bulk components, this method is well suited for an investigative synthesis of a novel material with controlled nanostructure. Our approach used pure HfO_2 ablation targets, with carbon supplied from acetylene (C_2H_2) background gas. The choice of C_2H_2 as the source of carbon was guided by its simple molecular structure and prior reports of efficient production of elemental carbon from C_2H_2 both in plasma and on hot surfaces.[24–26] Post-deposition annealing (PDA) at a relatively low temperature of 600 °C was used to reduce the content of hydrogenated carbon and enhance the sp^2 carbon–carbon bonding.

Details of the PLD synthesis of films with high carbon molar fractions are presented. Properties of the films are investigated using scanning electron microscopy (SEM), energy dispersive spectroscopy (EDS), X-ray photoelectron spectroscopy (XPS), Rutherford backscattering spectroscopy (RBS), hydrogen forward scattering (HFS), transmission electron microscopy (TEM), Raman spectroscopy, and X-ray diffraction (XRD). Based on this comprehensive sample characterization, it is established that, following PDA, the films represent a close analog of the carbon-rich hafnia interlayer that forms in oxidized HfC.

2. Experimental details

Pure sintered HfO_2 tablets with a nominal purity of 99.9%[27] were acquired from Cerac, Inc. and used as PLD targets. The targets were rotated at a rate of 20–30 rpm during film deposition. Silicon substrates were cleaved from an n-type Si(0 0 1) wafer. The target–substrate distance was 5 cm.

PLD was performed at room temperature in a stainless steel vacuum chamber evacuated by a turbomolecular pump, backed by a dry scroll pump. A continuous flow of C_2H_2 (99.6% purity, dissolved in acetone) was introduced into the chamber after reaching base pressure of about 7×10^{-5} Pa. The flow rate of C_2H_2 was regulated by an electronic mass flow controller, and the C_2H_2 pressure was measured by a capacitance pressure gauge. This paper reports synthesis and studies of films grown at three different C_2H_2 pressures – 0.08, 0.2, and 0.6 Pa – which resulted in films with different carbon molar fractions. Following PLD, substrates with films were cleaved into two parts and one of them was reattached to the heated substrate holder of the

PLD chamber using silver paint and subjected to PDA. Annealing was performed at 600 °C for 1 h in vacuo (base pressure $\sim 2 \times 10^{-4}$ Pa).

A XeCl excimer laser provided ~15 ns long pulses at a wavelength of 308 nm. The laser beam was tightly focused by a spherical lens onto the target at a 45° incident angle to achieve a fluence of about 3 J/cm^2. Prior to film deposition, the substrate was shielded by a movable shutter and target was pre-ablated for 10 min to remove any contamination from target surface. The laser was operated at a repetition rate of 2 Hz and the film growth rate was found to be about 0.1 Å/pulse.

The XPS analysis was performed using a PHI Quantum 2000 instrument equipped with a monochromated Al-K_α source ($h\nu = 1486.6$ eV). The analysis area was 1.4×0.3 mm. A large take-off angle (TOA) of 75° was used to maximize the depth of photoelectron detection and thus minimize the contribution of surface contaminants to the data.

The Raman spectra were collected on a Jobin Yvon LABRAM spectrometer equipped with an Olympus BX40 microscope using the backscattering geometry. An Ar^+ ion laser (514.5 nm wavelength) and a grating with 1800 g/mm were used in these measurements. The probe spot size was 1–2 μm. For each analyzed sample, the Raman spectra were collected for at least 3 different surface sites. No significant variation of the spectra with position was observed, except for the samples grown in 0.08 Pa of C_2H_2, as will be discussed later.

RBS was performed using He^{2+} ion beam with energy of 2.275 MeV. The incident ion trajectory was perpendicular to the sample surface and scattered ions were detected at a backscattering angle of 160°. In HFS experiments, the incident ion beam probed the sample at a grazing angle of 15°, while the detector counted hydrogen ions that were forward-scattered after collisions with the probing He^{2+} at an angle of 15° with respect to the surface. A thin absorber foil was placed over the detector to filter out the He^{2+} ions that were also forward-scattered. The hydrogen concentrations were determined by comparing the hydrogen ion counts from samples under investigation with those obtained from reference samples. A hydrogen-implanted silicon sample and a sample of muscovite with known hydrogen concentrations were used as references, To account for surface hydrogen due to residual moisture or hydrocarbon adsorption, a silicon control sample was analyzed together with the actual sample, and the signal from the control sample was subtracted from that from the actual sample. The estimated absolute experimental uncertainties of the atomic fractions determined by RBS/HFS are ±1 at% for Hf, ±3 at% for O, ±4 at% for C, and ±2 at% for H.

Imaging of the film surfaces was performed using a JEOL JSM-6700F field-emission scanning electron microscope equipped with an EDAX Genesis XM system for EDS microanalysis. Gold coating of the SEM samples was not needed, because the samples did not charge significantly under the electron beam. In contrast, reference samples of pure HfO_2 showed significant charging effects. This observation suggests that carbon-rich hafnia films have relatively high electrical conductivity. However, in the present study the conductivity was not measured.

Cross-sections of the films were imaged using a Tecnai F20 field-emission TEM equipped with an XT-type objective polepiece, and operating at an acceleration voltage of 200 keV. The TEM also comprises a Fischione High-Angle Annular Dark Field (HAADF) detector for scanning TEM imaging and an Oxford INCA EDS detector. The TEM samples were prepared by standard mechanical polishing using wedge-polishing technique. The final thinning as well as surface cleaning was performed by Ar^+ ion milling using GATAN PIPS system. A low energy beam (2–3 keV) and low milling angles (3–6°) were used.

XRD was performed using a Philips XRG 3100 powder diffractometer.

The reported values of the optical bandgap for HfO_2 are 5.6–5.9 eV, [28–32] hence pure HfO_2 is expected to be transparent for 308 nm ($h\nu = 4$ eV) radiation. However, in the present study it was found that white sintered HfO_2 targets had sufficiently high absorption at 308 nm to allow efficient ablation by the focused laser beam. This finding is not unexpected, given that sub-bandgap absorption in HfO_2 extending to energies as low as 4 eV has been reported and attributed to intrinsic defects of unidentified type.[29,33,34]

3. Results

Films with thicknesses of up to ~700 nm were deposited. Even the thickest films were stable and well-adhering even after annealing to 900 °C. This indicates that the films do not have significant strain and can tolerate a significant coefficient of thermal expansion mismatch with the Si substrate.

3.1. SEM imaging of the target and films

Fig. 1 shows SEM micrographs of pristine and ablated HfO_2 target surfaces, whereas the evolution of the target surface during pulsed laser ablation is shown in Fig. 2. Before ablation, the target shows a porous and rather loosely packed structure. The size of HfO_2 grains is in the range 50–300 nm (Fig. 1c). The spatially periodic ripples that develop after a considerable number of pulses (Fig. 2d) are indicative of transient melting followed by resolidification and they are commonly observed in laser ablation of various materials.[35] The porosity is practically removed after ablation and, instead, the surface develops narrow cracks (Fig. 1d) that seem to propagate along grain boundaries (Fig. 1e and f). Thus, although the initial target surface quality is rather poor, the ablation process itself acts to improve the target compactness. This fact may explain the virtual absence of contamination of the films by micron-size particulates, which is otherwise very common in PLD from ceramic targets.[35]

Fig. 3 shows an SEM image of the surface of a sample film. The only features on the otherwise remarkably smooth surface are round particulates, with diameters in the ~50–300 nm range. A weak increasing trend in the surface density of particulates with background C_2H_2 pressure was noticed. This pressure dependence and the relatively small size of particulates suggest that they are formed by nucleation and growth in the vapor phase (which is more effective when there are more collisions between

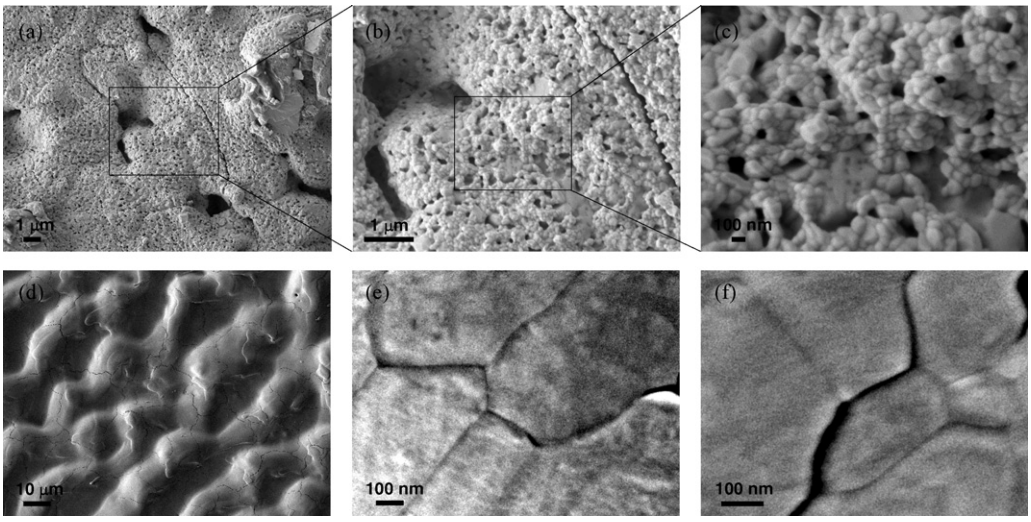

Fig. 1. SEM micrographs of the HfO_2 target surface before and after ablation. Pristine target surface is shown at different levels of magnification in images (a–c). Image (d) shows ablated surface with wavelike features and narrow cracks. Images (e) and (f) of the ablated surface show cracks that propagate along grain boundaries.

the vapor species and background gas), rather than from solidified liquid droplets expelled from the target (splashing).[35] The EDS spectrum of the scanned surface (Fig. 3c) shows a strong carbon peak, in addition to the expected Hf and O features, indicating significant incorporation of carbon in the film.

3.2. RBS and HFS analyses

Fig. 4 shows a typical RBS spectrum for a 160 nm thick film, together with the iteratively adjusted theoretical fit. For each C_2H_2 pressure the RBS analysis was performed on 2–3 samples deposited under nominally identical conditions, to assess the sample-to-sample variability of the composition. It was found that the composition uncertainty due to this variability was not larger than the experimental uncertainty of the RBS method. Fig. 5 provides a summary of the film compositions derived from RBS and Fig. 6 shows the positions of the films on the Hf–O–C composition diagram.

The O/Hf atomic ratio is less than 2 for all samples, although it approaches 2 for the lowest C_2H_2 pressure, which implies that the films contain oxygen-deficient HfO_{2-x}. The result is not surprising, given that oxygen defficiency is commonly observed in films of HfO_2 and other oxides grown in low-oxygen atmospheres.[33] As noted in the introduction, the interlayer oxide

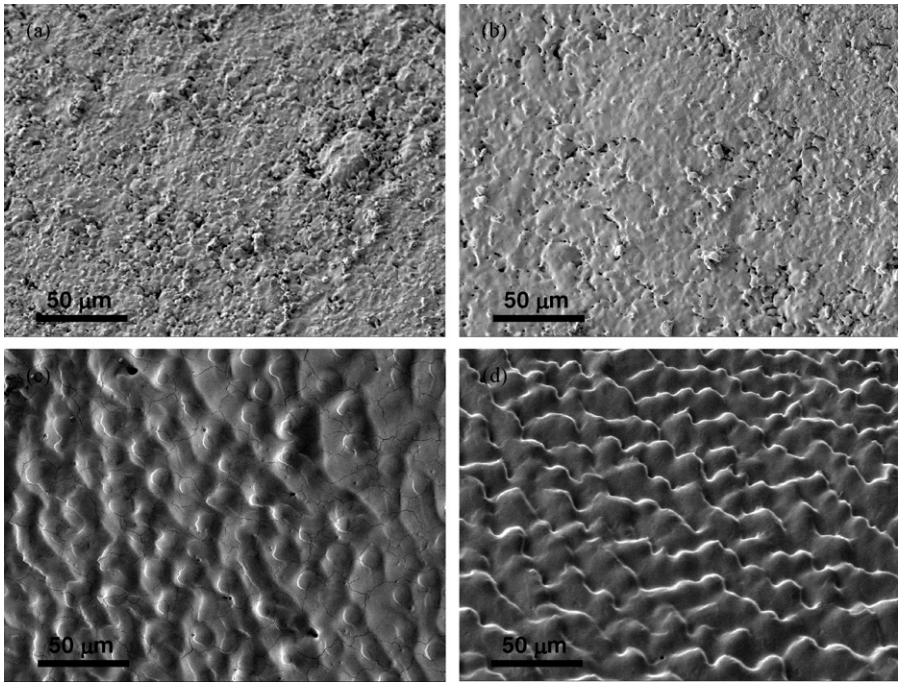

Fig. 2. SEM images showing evolution of the HfO_2 target surface during ablation: (a) pristine surface; (b) surface ablated by 1 laser pulse; (c) surface ablated by 10 pulses; (d) surface ablated by more than 100 pulses.

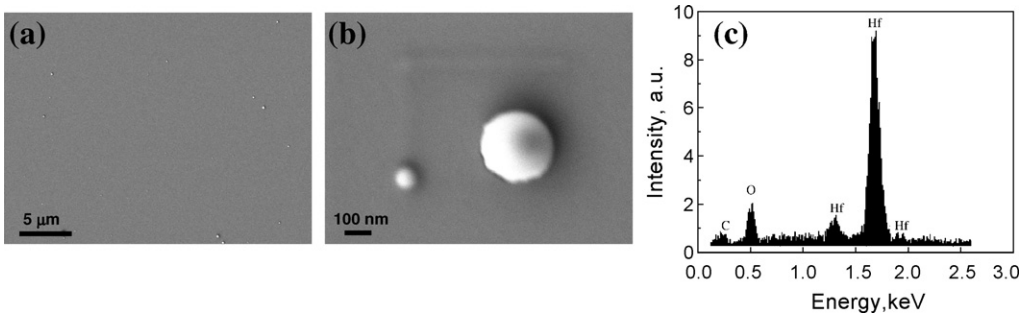

Fig. 3. (a) and (b) SEM micrographs of a film grown in 0.2 Pa of C_2H_2, showing nearly spherical sub-micron particles; (c) EDS spectrum of the film surface shown in (a).

$HfO_{2-x}C_y$ that is the model for this study is also oxygen-deficient. The O/Hf ratio seems to decrease with the C_2H_2 pressure, possibly because C_2H_2 acts as an oxygen scavenger. The C/Hf atomic ratio in the films increases rapidly with the C_2H_2 pressure, and its pressure dependence is consistent with the linear one in the range covered in this work (Fig. 5).

Given that the source of carbon used in this study is a hydrocarbon, the presence of hydrogen in the films was anticipated, and the HFS measurements confirmed it. Fig. 7 shows HFS spectra of a film before and after annealing at 600 °C. The atomic concentration of H decreased from about 5% to 1.4% after annealing (Table 1 provides stoichiometry of these samples). Most of the hydrogen is probably present within various forms of hydrogenated carbon, as will be elaborated in Section 3.5 that discusses Raman spectroscopy studies of the films.

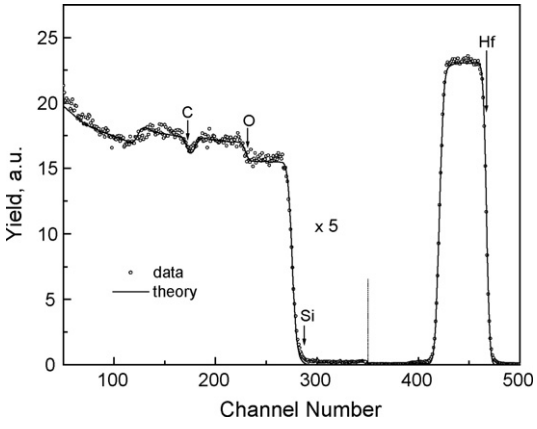

Fig. 4. RBS spectrum of a film grown in 0.6 Pa of C_2H_2.

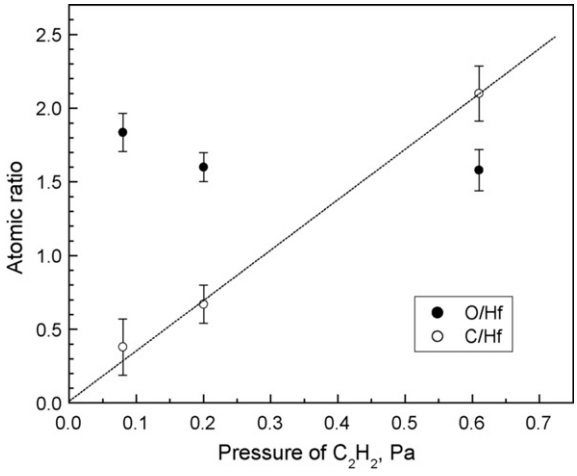

Fig. 5. The O/Hf and C/Hf atomic ratios obtained by RBS as functions of the C_2H_2 pressure used during PLD. The error bars represent the RBS experimental uncertainties and the dashed line is guide to the eye.

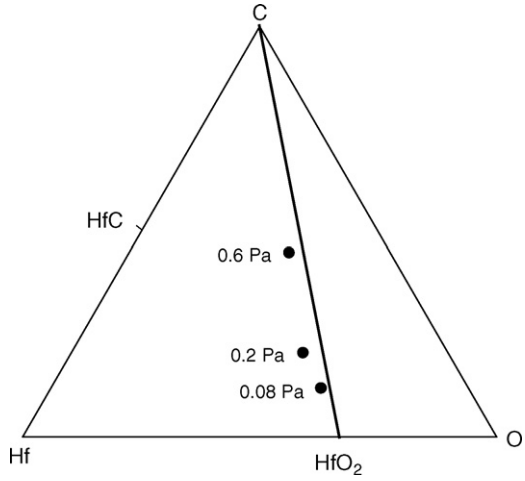

Fig. 6. The three film compositions studied in this work. The numbers next to symbols denote the C_2H_2 pressures used during PLD.

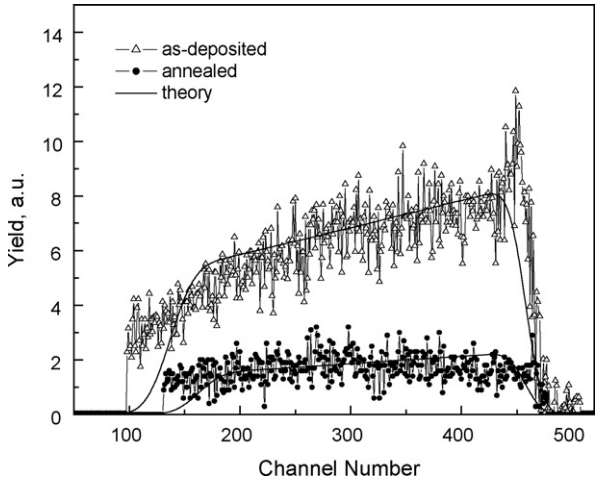

Fig. 7. HFS spectra of a film grown in 0.2 Pa of C_2H_2 (upper curve) and of the same film after annealing at 600 °C (lower curve).

Table 1
Summary of the XPS and RBS/HFS data for a film grown in 0.2 Pa of C_2H_2 and for the same film after annealing at 600 °C.

Method	Chemical state	As-deposited % of total C, O, or Hf	Annealed % of total C, O, or Hf
XPS C 1*s*	C–C, C–H	75	85
	Carbide	6	4
	C–O	11	6
	C═O	4	3
	O–C═O	5	3
XPS Hf 4*f*	HfO_2 or HfO_{2-x}	86	100
	HfC_xO_y (oxycarbide)	8	0
	HfC	6	0
XPS O 1*s*	HfO_2	75	85
	Organic	25	15
Stoichiometry from XPS, total		$HfO_{1.99}C_{2.55}$	$HfO_2C_{1.86}$
Stoichiometry from XPS, corrected[a]		$HfO_{1.73}C_{2.22}$	$HfO_{1.7}C_{1.58}$
Stoichiometry from RBS and HFS		$HfO_{1.6}C_{0.67}H_{0.15}$	$HfO_{1.75}C_{0.7}H_{0.05}$

[a] The corrected stoichiometry was calculated by taking into account only the fractions of Hf and O bonded as HfO_{2-x} and the fraction of C bonded as C–C or C–H.

Fitting of the RBS spectra by a theoretical model requires iterative adjustment of the elemental densities and sample thickness until good agreement with the data is obtained. For those samples for which both the TEM and RBS analyses were performed, a good agreement was found between the sample thickness observed in TEM and that derived by RBS data fitting. Therefore, the atom densities derived from RBS can be used quite reliably to estimate the film mass densities. For films deposited in 0.08, 0.2, and 0.6 Pa of C_2H_2, mass densities of 7.2, 7.7, and 6.7 g/cm^3, respectively, were found, with an estimated uncertainty of about 10%. No significant densification upon PDA at 600 °C was found within the method's uncertainty limits.

3.3. XPS analysis

A typical XPS survey spectrum of a sample film is shown in Fig. 8. In addition to Hf, O, and C, the only elements detected are Zr (typically 0.1% or less) and F (0.2–1.3%). The presence of Zr was expected, as it is a common substitutional impurity in Hf compounds and was identified in the elemental analysis of our PLD targets. The origin of the F impurity is unknown, and it was introduced either during film growth as an impurity in C_2H_2 background gas, or in the post-deposition sample handling. High-resolution XPS spectra, not shown here, indicated that Zr was present as ZrO_2, while F bonding is consistent with that of inorganic or organic fluorides.

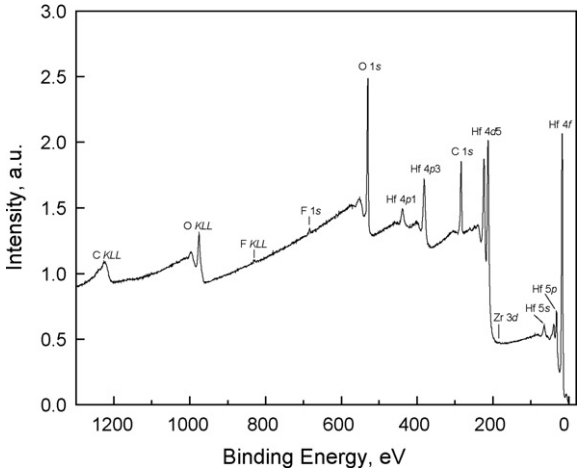

Fig. 8. Typical XPS survey spectrum of an $HfO_{2-x}C_y$ film.

Representative high-resolution XPS spectra in the Hf 4*f*, C 1*s*, and O 1*s* regions for a film grown in 0.2 Pa of C_2H_2 and the same film after PDA in vacuo at 600 °C are shown in Fig. 9. A summary of the chemical states identified in these spectra is provided in Table 1. The analysis indicates that Hf is bonded predominantly to O, whereas the principal peak of C is consistent with both carbon- and hydrogen-bonded carbon. The principal state of oxygen is consistent with HfO_2 bonding. The position of the main Hf 4*f* doublet observed in our XPS spectra is somewhat shifted to lower energies compared with the values that are most commonly reported for fully oxidized HfO_2, which indicates that the oxide is oxygen-deficient HfO_{2-x},[36] consistent with the RBS result.

The minor chemical states detected in the film suggest the presence of organic impurities and, possibly, Hf carbide and oxycarbide (Table 1). A probable source of the organics is surface contamination that occurred after deposition. Organics may also be present in the bulk (the estimated probe depth of XPS at a 75° TOA is up to 10 nm), introduced by impurities (such as acetone) that are present in C_2H_2, or produced in reactions of the products of C_2H_2 decomposition with oxygen species ablated from the target. Signatures of carbon–carbon triple bonding that would be indicative of residual C_2H_2 trapped in the film were not observed. The main C 1*s* peak may have a significant contribution from surface contamination by hydrocarbons, as will be discussed below.

After annealing, the contributions of organic-bonded O and oxygen-bonded C decrease significantly, while the Hf 4*f* spectrum does not show indications of any states other than HfO_{2-x}. The result suggests that annealing removes significant fraction of the organic constituents, probably via thermal decomposition and subsequent effusion or re-bonding of decomposition

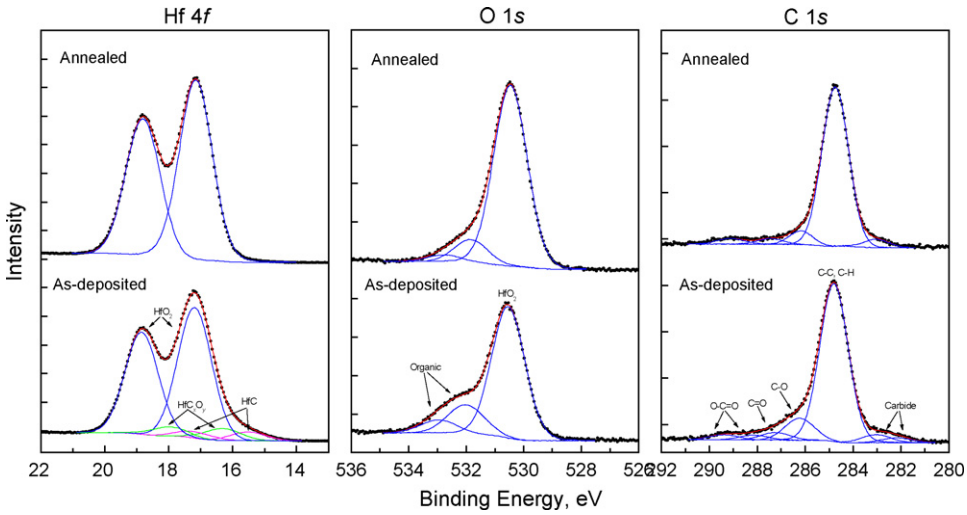

Fig. 9. High-resolution XPS spectra of a film grown in 0.2 Pa of C_2H_2 (lower curves) and of the same film after annealing at 600 °C (upper curves). Symbols represent experimental data, red curves represent cumulative multi-peak fits, and curves in other colors represent individual (Gaussian-like) peaks in the fit.

products. As noted above, Hf oxide is oxygen-deficient, implying that Hf dangling bonds are present; therefore, oxygen atoms produced by decomposition of organics are likely to bond with Hf. Likewise, it is possible that the carbon atoms and hydrocarbon radicals released from organics subsequently bond into larger hydrocarbon or elemental carbon structures.

Table 1 provides stoichiometries, as derived from RBS/HFS, for the films whose XPS spectra are shown in Fig. 9, together with the stoichiometries that were calculated from XPS peak signals in two ways. The "stoichiometry from XPS, total" was calculated using total atomic percentages of Hf, O, and C derived from XPS peak intensities. The "stoichiometry from XPS, corrected" takes into account only the fractions of the three elements that are derived from the dominant XPS peaks, i.e., the fractions of Hf and O that are bonded as HfO_{2-x} and the fraction of C that is bonded as C–C or C–H. The "total" XPS stoichiometry has an O/Hf atomic ratio near 2, and a very high percentage of C. The "corrected" XPS stoichiometry has an O/Hf ratio that is very close to the one derived from RBS; however, the corrected carbon fraction is still considerably higher than that derived from RBS. This result is interpreted as follows. XPS signal is always affected by surface contamination, thus the higher oxygen content found by XPS is partly due to organic impurities (and, possibly, water) that are mostly concentrated in the surface region, which distorts the O/Hf ratio in XPS while not contributing significantly to the RBS data. Thus, by eliminating the contribution of organic chemical states in O 1*s* and Hf 4*f* from the stoichiometry calculation, the correct O/Hf ratio is obtained. Hydrocarbon contaminants are also concentrated in the surface region. However, their contribution to the C–C, C–H peak in XPS is impossible to decouple from the C–C, C–H signal due to elemental carbon and hydrocarbons in the bulk, thus the overestimate of C atomic fraction remains in the corrected XPS stoichiometry.

3.4. Film microstructures

Fig. 10 shows a bright-field TEM (BFTEM) image of the cross-section of a 680 nm thick as-deposited film, as well as a high-resolution TEM (HRTEM) image of the region adjacent to the Si substrate with the corresponding selected-area electron diffraction (SAED) pattern. The structure of the film is clearly

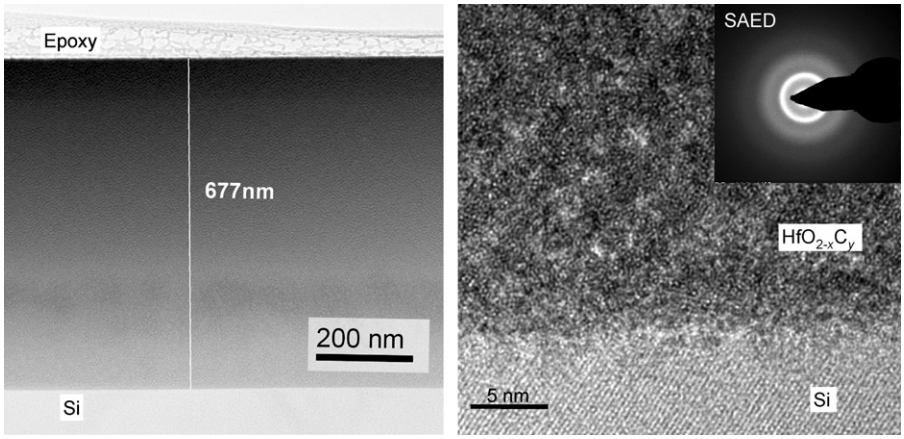

Fig. 10. Left: BFTEM image of the cross-section of an $HfO_{2-x}C_y$ film grown in 0.6 Pa of C_2H_2. Right: HRTEM image of the region adjacent to Si substrate. Inset: SAED pattern of the film.

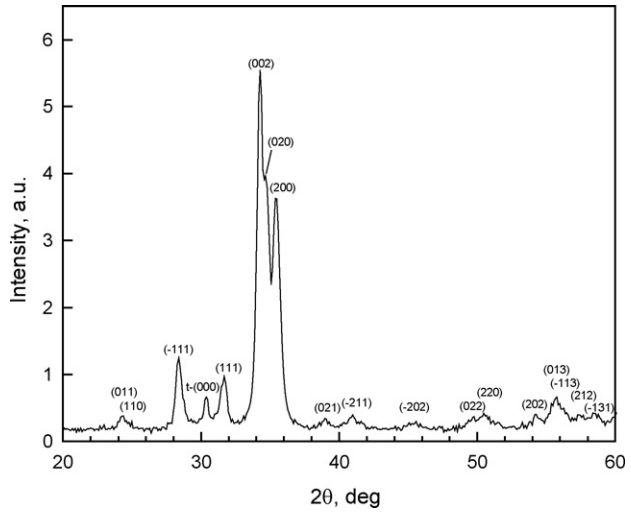

Fig. 11. XRD pattern of a film grown in 0.08 Pa of C_2H_2 and annealed at 600 °C. In this film with low carbon content, annealing caused crystallization of HfO_2. All the peaks are assigned to the monoclinic phase of HfO_2 except the peak labeled "t-(0 0 0)", which is assigned to the tetragonal phase.

disordered, with neither HfO_2 nor carbon forming nanocrystallites and a SAED pattern that shows only diffuse rings due to short-range ordering. TEM of other as-deposited samples showed very similar microstructures. The EDS analysis on TEM performed for a number of different spots in a film cross-section always showed peaks of all three main constituent elements (Hf, O, and C), with relative peak intensities that did not vary significantly from spot to spot. Given that the estimated resolution of the EDS spot analysis is ~5 nm, this result indicates that carbon and HfO_2 are mixed on a very short length scale.

The microstructures of annealed films showed strong dependence on the carbon molar fraction. For the films grown in 0.2 and 0.6 Pa of C_2H_2, after PDA the microstructures were virtually unchanged, with featureless XRD patterns and no indications of microcrystallinity or phase separation between HfO_2 and carbon in TEM images. However, annealing of films grown in 0.08 Pa of C_2H_2 caused crystallization of HfO_2. The XRD pattern, Fig. 11, shows that HfO_2 crystallized in the expected monoclinic phase. The intensities of peaks (0 0 2), (0 2 0) and (2 0 0) are several times higher than is expected for randomly oriented crystallites, indicating that HfO_2 crystallites form with these orientations as preferred ones. The origin of this preferred orientation is currently not understood. The average size of crystallites, determined from XRD peak broadening, was found to be about 16 nm.

One of the XRD peaks found is not consistent with the monoclinic phase, but it can be assigned to the (0 0 0) plane of the tetragonal phase (Fig. 11). Other tetragonal phase peaks were not observed, hence it cannot be asserted that the tetragonal phase is indeed present. It is possible that (0 0 0) is the preferred orientation for growth of tetragonal crystallites, which would explain the enhanced intensity of the (0 0 0) diffraction. At any rate, while the stable phase of bulk HfO_2 at room temperature is the monoclinic one, the presence of minor tetragonal phase is possible when the crystalline HfO_2 is formed by annealing from amorphous HfO_2. In fact, published work indicates that crystallization of HfO_2 into tetragonal phase seems to be preferred when the amorphous precursor has a large surface area[37] and when long-range structural order is inhibited by geometrical constraints[38] or by mixing with other oxides.[39,40]

Films of pure HfO_2 grown by PLD at room temperature are typically amorphous,[41] and it is thus not surprising that the as-deposited films studied here are amorphous as well. However, in pure HfO_2 films the development of microcrystallinity upon PDA is expected for annealing temperatures as low as 400–450 °C.[42–44] As the contrasting annealing behavior of films with different C/Hf ratios shows, high carbon content has the effect of stabilization of the amorphous structure of HfO_2, and with a C/Hf ratio ≥0.65 (Fig. 5) crystallization is inhibited to at least 600 °C.

3.5. Raman spectroscopy

Raman spectroscopy provided key insights into the form of carbon present in the films. The Raman spectra of disordered carbons that contain sp^2 bonds show two characteristic features: the G band around 1560 cm^{-1}, which is due to the stretching vibrations of pairs of sp^2 C atoms in both rings and chains (E_{2g} mode)[45,46]; and the D band around 1360 cm^{-1}, which is forbidden in perfect graphite and appears in the presence of disorder due to double resonant Raman scattering.[47] For various forms of carbon, the ratio of integrated intensities of the D and G peaks, I_D/I_G, has been commonly used to assess the carbon structural ordering.[45,48–51] The ratio is related to the average size of graphitic clusters (in-plane correlation length), L_a, via the Tuinstra-Koenig (TK) relation $I_D/I_G = C(\lambda)/L_a$,[46] where λ is the excitation wavelength. For $\lambda = 514.5$ nm, C ~44 Å.[46,48] Another parameter used to characterize the carbon bonding is the full width at half maximum of the G peak ($FWHM_G$), which increases as disorder increases.[48,52,53]

The Raman spectra for as-deposited and annealed films grown in 0.08 Pa of C_2H_2 are shown in Fig. 12. The spectrum for the as-deposited film shows only a weak, very broad band in the region 1000–1600 cm^{-1}, which cannot be assigned to any form of carbon, and is possibly a second-order spectral feature due to phonon scattering of the amorphous HfO_2 film.[54] The strong band at 960 cm^{-1} is due to optical phonon scattering of the Si substrate.[55] For the annealed sample, it was found that the spectra were strongly dependent on the position on the sample surface—a behavior not observed for samples with higher carbon contents. For all surface spots probed, the spectra show a baseline that increases with the Raman shift. This is the photoluminescence (PL) background that is a well-known signature of various forms of amorphous hydrogenated carbon (a-C:H).[52,56] The PL background is expected to increase with the H content, due to the hydrogen saturation of nonradiative recombination centers,[56] and for carbons with H atomic contents over ~45% the background usually overshadows the Raman features of a-C:H.[45,53,56] These carbons are usually referred to as polymer-like a-C:H (PLCH) and they are characterized by a high fraction of sp^3 bonds, which are mostly H-terminated.[52] Notwithstanding the similarity between the Raman spectra of PLCH and that of the annealed carbon-rich hafnia film in Fig. 12, the two carbon

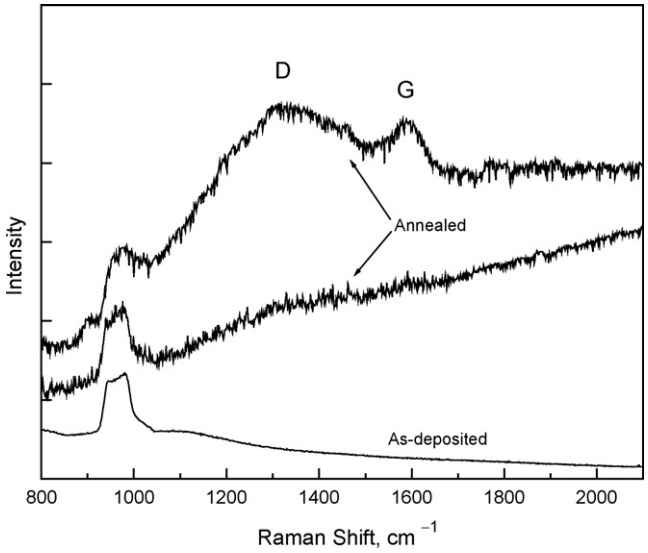

Fig. 12. Raman spectra of a film grown in 0.08 Pa of C_2H_2 (bottom curve) and of the same film after annealing at 600 °C, probed at two different surface locations (upper two curves). The upper two curves have been shifted in the vertical direction for clarity. Labels "D" and "G" denote the respective vibrational modes of sp^2 carbon.

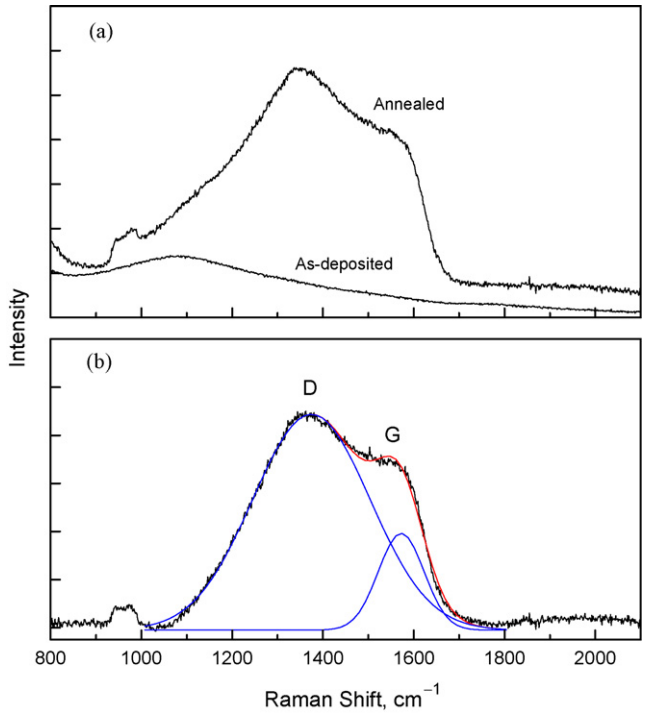

Fig. 13. Raman spectra of an $HfO_{2-x}C_y$ film grown in 0.2 Pa of C_2H_2: (a) spectra measured before and after annealing at 600 °C; (b) background-subtracted experimental spectrum for the annealed film (black curve) is shown together with the cumulative two-peak Gaussian fit (red curve) and the individual Gaussians (blue curves).

systems are obviously very different; the film has an H/C atomic ratio less than 0.1, which is much lower than the ratios (∼1) characteristic for PLCH. Unlike hydrogenated carbon in PLCH, carbon in here studied films is trapped within a HfO_{2-x} matrix, which may inhibit formation of sp^2-bonded carbon domains and cause the sp^2 Raman features to be much weaker than what would be expected for pure hydrogenated carbon.

Upon annealing of hydrogenated carbons at 600 °C, significant effusion of bonded hydrogen is expected, leading to loss of hydrogen from samples.[53,57] The HFS measurements that were presented above confirmed significant hydrogen loss, while no significant carbon loss on PDA in vacuo was detected. Given that as-deposited films contain more hydrogen then annealed ones, it is not obvious why the film deposited at 0.08 Pa of C_2H_2 shows the PL background characteristic for a-C:H only after PDA. A probable reason for this is that the as-deposited film, given the low overall carbon concentration in it, actually contains mostly small hydrocarbon molecules and, possibly, small clusters or elemental carbon. In contrast to extended structures of a-C:H, these smaller species of carbon do not produce the PL background. Annealing leads to a reduction in hydrogen content and reordering of carbon into extended networks of a-C:H, characterized by the PL. This is probably accompanied by enhanced ordering of the existing sp^2 phase and the conversion of some sp^3 sites into sp^2 sites.[57,58]

For some probed spots, the Raman spectra of the annealed film grown in 0.08 Pa of C_2H_2 show the D and G peaks in addition to the PL background (Fig. 12), indicating that at these locations the H content is lower and/or the fraction of sp^2 carbon is higher than in the spots that do not show these peaks. The non-uniformity in the spatial distribution of hydrogenated carbon observed in the annealed film is probably related to HfO_2 crystallization, discussed in Section 3.4. The formation of HfO_2 crystallites is expected to augment any inherent non-uniformity of the carbon distribution that had been present in the film before crystallization took place. The regions with lower initial carbon concentration crystallize earlier and form larger crystallites, which drives the migration of carbon to neighboring spatial regions. Therefore, it is plausible that crystallization of HfO_2 leads to coalescence of carbon domains, and in these enlarged domains the formation of extended sp^2 carbon chains and rings is likely at 600 °C. Surface spots that contain such carbon will thus have enhanced D and G peaks.

For those spatial regions that did produce Raman spectra with the D and G peaks (Fig. 12), the relative integrated intensities (areas) of the two peaks were estimated. After subtracting the PL baseline from the spectra, 2-peak Gaussian fits to the data were performed (an example of such a fit is shown in Fig. 13). The average I_D/I_G ratio thus obtained (Table 2) is very high, and using the TK formula a sub-nanometer graphite cluster size is obtained. It has been argued[45] that the TK formula is not applicable for clusters smaller than ∼2 nm, hence the use of this approach to estimate the cluster sizes is not self-consistent for the samples studied here. Therefore, the I_D/I_G parameter is here not used for quantitative estimate of the graphite cluster sizes, and its values are listed in Table 2 only as a reference and without further analysis.

The Raman spectra for the as-deposited and annealed films deposited in 0.2 Pa of C_2H_2 are shown in Fig. 13. The as-deposited sample spectrum again does not show any carbon features. However, the annealed sample spectrum shows much

Table 2
Parameters derived by fitting the G and D Raman peaks and the proposed form of carbon in the films. I_G and I_D are the peak areas and $FWHM_G$ is the width of the G peak. The uncertainties represent standard deviations of multiple measurements in which different spots of the film surfaces were probed. PLCH, DLCH, and GLCH denote polymer-like, diamond-like, and graphite-like amorphous hydrogenated carbon, respectively.

C_2H_2 pressure (Pa)	Sample	I_D/I_G	$FWHM_G$ (cm^{-1})	Proposed form of carbon in the films
0.08	As-deposited	–	–	Hydrocarbons, small C clusters
	Annealed[a]	6.7 ± 1.3	86 ± 16	PLCH
0.2	As-deposited	–	–	Hydrocarbons, small C clusters
	Annealed	10 ± 1	96 ± 11	GLCH or nano-graphitic
0.6	As-deposited	2.32 ± 0.04	107 ± 2	DLCH
	Annealed	3.4 ± 0.2	74 ± 3	GLCH or nano-graphitic

[a] For this sample not all of the surface spots probed produced G and D peaks (see text).

stronger sp^2 carbon features than those observed in the sample deposited at the lower C_2H_2 pressure, and the PL background contribution is negligible. This spectrum is similar to those of a-C:H with a hydrogen content less than 20%, usually referred to as the graphite-like a-C:H (GLCH).[52] Given that the RBS/HFS data indicate that not more than 7% of carbon in this annealed sample is hydrogenated (Table 1), carbon in this film may also be categorized as nano-graphitic.

For films grown in 0.6 Pa of C_2H_2, the signatures of graphitic carbon are present even before annealing (Fig. 14). Based on a qualitative comparison of the sizes of sp^2 carbon peaks with that of the PL background, the spectrum is very similar to those of a-C:H with an intermediate (20–40%) H content and a lower sp^3 content than that of PLCHs, in the literature referred to as the diamond-like a-C:H (DLCH).[52] After annealing, the sample shows well-defined G and D peaks, consistent with the behavior of GLCH or nano-graphitic carbons.

The width of the G peak, $FWHM_G$, decreases with annealing for films grown in 0.6 Pa of C_2H_2 (Table 2). This indicates increased ordering of the sp^2 regions that accompanies the effusion of hydrogen species. A weak decreasing trend in $FWHM_G$ with increasing carbon content in the annealed films is also suggested (Table 2). The relatively low value of $FWHM_G$ for the annealed film deposited at the lowest C_2H_2 pressure, which breaks the latter trend, is not representative of the entire film, but of selected regions, as discussed above. The increase of the sp^2 ordering with C content in the annealed films possibly results from better initial ordering in as-deposited films with higher C concentration, given that higher surface density of C adatoms implies higher probability of formation of extended sp^2 chains and rings.

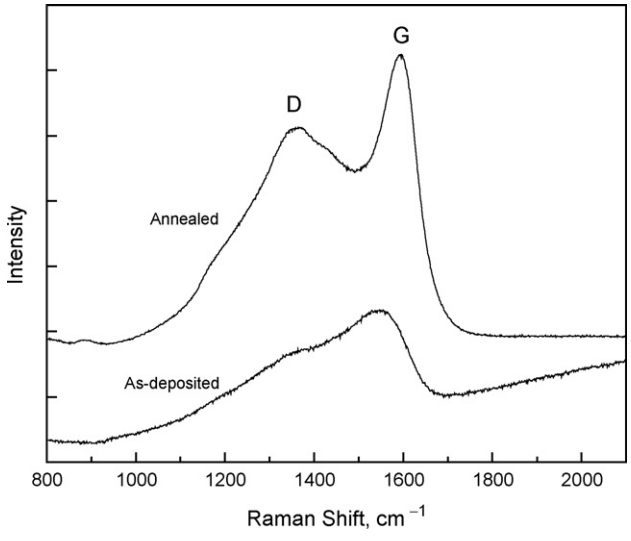

Fig. 14. Raman spectra of a film grown in 0.6 Pa of C_2H_2 (lower curve) and of the same film after annealing at 600 °C (upper curve). The upper spectrum has been shifted in the vertical direction for clarity.

4. Discussion

It was demonstrated that very high fractions of carbon are incorporated in the films even with low C_2H_2 background pressures, and here possible mechanisms for carbon incorporation are discussed. To estimate the total number of carbon atoms available for inclusion in a film by each laser pulse, let us consider a conical volume whose apex is at the laser spot on the target and the base of unit area (1 cm^2) is at the substrate. Taking a C_2H_2 pressure of 0.2 Pa and the target–substrate distance of 5 cm, at room temperature this volume contains 8.16×10^{13} C_2H_2 molecules, or 1.63×10^{14} C atoms. The RBS analysis found that the number density of C atoms in films deposited at this C_2H_2 pressure was about 1.45×10^{22} cm^{-3}, while the film growth rate estimated from the RBS/TEM film thickness and the number of laser pulses was about 1.2×10^{-9} cm/pulse. Multiplying the last two numbers, it follows that, after each pulse, about 1.7×10^{13} C atoms are deposited per 1 cm^2 of substrate. Therefore, about 11% of the C atoms that were initially contained within the conical volume as C_2H_2 become incorporated in the film after each pulse.

No evidence was found of triply bonded carbon in the films, indicating that trapping of C_2H_2 during film growth is not a significant source of carbon. This implies that C_2H_2 is decomposed by one or more processes during laser ablation and the products of decomposition (and, possibly, subsequent reactions) are carried towards the substrate by the laser plume. The 308 nm photon energy is insufficient for photodissociation of C_2H_2 in a single-photon process.[59] The carbon molar fraction in the films did not show significant dependence on the laser fluence, indicating that multiphoton photodissociation processes are insignificant as well. The remaining possible routes for C_2H_2 decomposition in the system include (i) thermal decomposition at and near the target surface that is transiently heated by laser pulses, (ii) thermal decomposition in the ablation plume plasma, and

(iii) decomposition by impact with energetic particles in the plume.

The route (i) seems insignificant, given that the number of C_2H_2 molecules in the vicinity of laser-heated spot at the target is a small fraction of the molecules contained within the ablation cone discussed above. In addition, the EDS analysis of the ablated target surface did not indicate the presence of carbon, which would be expected if significant C_2H_2 decomposition at the target surface were taking place. Therefore, decomposition routes (ii) and (iii) are the most plausible sources of carbon in the films. The products of C_2H_2 decomposition (C, C_2, CH, etc.) are likely to react upon reaching the substrate (or film) surface, given their high number density. The products of these reactions may include elemental carbon in various forms and hydrocarbons. How extensive bonding will take place at the surface depends on the surface density and mobility of adatoms. Thus, larger elemental and hydrogenated carbon structures are expected for higher C_2H_2 pressures and higher substrate temperatures.

Based on the presented results of comprehensive analyses of the films, the following description is proposed. Upon deposition, Hf and O in the films are present predominantly as amorphous HfO_{2-x}. In samples with low overall carbon concentration, carbon is deposited largely in the form of hydrocarbons or small clusters of elemental carbon, with a small fraction bonded within organic impurities. In samples with high carbon concentration, upon pulsed deposition a more extended sp^2 and sp^3 bonding occurs between C adatoms, and the films contain disordered networks of hydrogenated carbon with an intermediate content of sp^3 bonds, similar to those in DLCHs.

Annealing greatly reduces the amount of both organics and hydrogen in the films. This is probably caused by thermal decomposition of organics and some hydrocarbons and subsequent effusion of the products of this decomposition. Thermal effusion measurements of a-C:H films have shown that the peak of effusion occurs at 600 °C, and the main effusion species is H_2, while minor species include H, CH_4, C_2H_4, CH_3, and other hydrocarbons.[57] It is likely that elemental hydrogen is the dominant effusion species in our films as well, given that annealing significantly reduces the H content, while the C content is not affected significantly. Hydrogen loss is accompanied by the conversion of sp^3 sites into sp^2 sites, as has been reported for annealed a-C:H.[57,58,60] In addition, ordering in the existing sp^2 regions is improved and it is likely that some neighboring sp^2 regions coalesce. This structural evolution of carbon is reflected in the enhanced sp^2 vibrational modes and, in particular, sharpening and increase of the Raman D peak.

5. Conclusions

High-quality films of hafnia with very high carbon contents were synthesized. The carbon fraction in the films can be easily controlled by varying the background C_2H_2 pressure during PLD. Upon annealing at 600 °C, carbon in the films is present predominantly as GLCH or nano-graphitic carbon, while Hf and O are bonded almost exclusively within oxygen-deficient dioxide. The films have very finely grained microstructures and nanocrystallinity is inhibited to at least 600 °C for films with the two higher carbon fractions. The results indicate that the annealed films present close analogs of the $HfO_{2-x}C_y$ oxide interlayers formed in oxidation of HfC.

Our current and future studies of the $HfO_{2-x}C_y$ system will investigate the stabilization of the amorphous structure of the films at higher annealing temperatures and determine the behavior of the material in oxidizing environments.

Acknowledgements

D.A.P. acknowledges funding by the Air Force Office of Scientific Research (AFOSR) under contract FA9550-07-C-0046. The work at Vanderbilt University was funded through AFOSR contract FA9550-04-1-0448. D.A.P. thanks Dr. Lorenza Moro for providing the XRD data. The authors acknowledge Drs. Robert Geil and Benjamin Schmidt for providing preliminary RBS and XPS data, respectively.

References

1. Raj R, Riedel R, Soraru GD. *J Am Ceram Soc* 2001;**84**:2158–9.
2. Sorary GD, Modena S, Guadagnino E, Colombo P, Egan J, Pantano C. *J Am Ceram Soc* 2002;**85**:1529–36.
3. Kroke E, Li YL, Konetschny C, Lekomte E, Fasel C, Riedel R. *Mater Sci Eng R-Rep* 2000;**26**:97–147.
4. Morcos RM, Navrotsky A, Varga T, Ahn D, Saha A, Poli F, Müller K, Raj R. *J Am Ceram Soc* 2008;**91**:2391–3.
5. Ferraioli L, Ahn D, Saha A, Pavesi L, Raj R. *J Am Ceram Soc* 2008;**91**:2422–4.
6. Raj R, An L, Shah S, Riedel R, Fasel C, Kleebe H-J. *J Am Ceram Soc* 2001;**84**:1803–10.
7. Fan Y, Zhang L, Jiang D, An L. *J Am Ceram Soc* 2004;**87**:48386.
8. Blum YD, MacQueen DB, Kleebe H-J. *J Eur Ceram Soc* 2005;**25**:143–9.
9. Resta N, Kohler C, Trebin H-R. *J Am Ceram Soc* 2003;**86**:1409–14.
10. Saha A, Raj R, Williamson DL. *J Am Ceram Soc* 2006;**89**:2188–95.
11. Varga T, Navrotsky A, Moats JL, Morcos RM, Poli F, Müller K, Saha A, Raj R. *J Am Ceram Soc* 2007;**90**:3213–9.
12. Bargeron, C.B., Benson, R.C. and Jette, A.N. NASA CP-3054, Part 3051. *National Aeronautics and Space Administration*, Washington, DC; 1989; p. 3083–3094.
13. Bargeron CB, Benson RC. *Surf Coat Technol* 1988;**36**:111–5.
14. Bargeron CB, Benson RC, Jette AN, Phillips TE. *J Am Ceram Soc* 1993;**76**:1040–6.
15. Bargeron CB, Benson RC, Newman RW, Jette AN, Phillips TE. *J Hopkins APL Tech D* 1993;**14**:29–35.
16. Shimada S, Inagaki M, Matsui K. *J Am Ceram Soc* 1992;**75**:2671–8.
17. Shimada S, Inagaki M, Suzuki M. *J Mater Res* 1996;**11**:2594–7.
18. Shimada S, Ishii T. *J Am Ceram Soc* 1990;**73**:2804–8.
19. Shimada S, Nakajima K, Inagaki M. *J Am Ceram Soc* 1997;**80**:1749–56.
20. Shimada S, Nishisako M, Inagaki M, Yamamoto K. *J Am Ceram Soc* 1995;**78**:41–8.
21. Shimada S, Yunazar F, Otani S. *J Am Ceram Soc* 2000;**83**:721–8.
22. Wuchina, E., Opeka, M. *In High temperature corrosion and materials chemistry*: Per Kofstad Memorial Symposium, Pennington, NJ, 2000; McNallan, M., Opila, E., Maruyama, T., Narita, T., editors. The Electrochemical Society Proceedings Series: Pennington, NJ, 2000; p. 477.
23. Sacks MD, Wang C-A, Yang Z, Jain A. *J Mater Sci* 2004;**39**:6057–66.
24. Ren ZF, Huang ZP, Xu JW, Wang JH, Bush P, Siegal MP, Provencio PN. *Science* 1998;**282**:1105.
25. de Graaf A, van Hest MFAM, van de Sanden MCM, Letourneur KGY, Schram DC. *Appl Phys Lett* 1999;**74**:2927–9.
26. Shang NG, Au FCK, Meng XM, Lee CS, Bello I, Lee ST. *Chem Phys Lett* 2002;**358**:187–91.

27. Spectrographic analysis showed that the main impurities in the HfO_2 tablets were: Zr (<0.5%); Zn (0.01%); Si (<0.002%); and Pb (<0.001%).
28. Afanas'ev VV, Stesmans A, Chen F, Shi X, Campbell SA. *Appl Phys Lett* 2002;**81**:1053–5.
29. Cho YJ, Nguyen NV, Richter CA, Ehrstein JR, Lee BH, Lee JC. *Appl Phys Lett* 2002;**80**:1249–51.
30. Balog M, Schieber M, Michman M, Patai S. *Thin Solid Films* 1977;**41**:247–59.
31. Callegari A, Cartier E, Gribelyuk M, Okom-Schmidt HF, Zabel T. *J Appl Phys* 2001;**90**:6466–74.
32. Aarik J, Mändar H, Kirm M, Pung L. *Thin Solid Films* 2004;**466**:41–7.
33. Ito T, Maeda M, Nakamura K, Kato H, Ohki Y. *J Appl Phys* 2005;**97**:054104.
34. Lucovsky G, Seo H, Fleming LB, Luning J, Lysaght P, Bersuker G. *Surf Sci* 2007;**601**:4236–41.
35. Chrisey DB, Hubler GK, editors. *Pulsed laser deposition of thin films*. New York: John Wiley & Sons; 1994.
36. Ratzke M, Kappa M, Wolfframm D, Kouteva-Arguirova S, Reif J. *Proc SPIE* 2004;**5662**:406–11.
37. Ushakov SV, Navrotsky A, Yang Y, Stemmer S, Kukli K, Ritala M, Leskela MA, Fejes P, Demkov A, Wang C, Nguyen B-Y, Triyoso D, Tobin P. *Phys Stat Solidi* 2004;**241**:2268–78.
38. Zhong L, Daniel WL, Zhang Z, Campbell SA, Gladfelter WL. *Chem Vapor Depos* 2006;**12**:143–50.
39. Afify ND, Dalba G, Koppolu UMK, Armellini C, Jestin Y, Rocca F. *Mater Sci Semicon Proc* 2006;**9**:1043–8.
40. Ushakov SV, Brown CE, Navrotsky A, Demkov A, Wang C, Nguyen B-Y. *Mater Res Soc Symp Proc* 2003;**745**:3.
41. Essary C, Howard JM, Craciun V, Craciun D, Singh RK. *Thin Solid Films* 2004;**450**:111–3.
42. Böscke TS, Govindarajan S, Kirsch PD, Hung PY, Krug C, Lee BH, Heitmann J, Schröder U, Pant G, Gnade BE, Krautschneider WH. *Appl Phys Lett* 2007;**91**:072902.
43. Zhu WJ, Tamagawa T, Gibson M, Furukawa T, Ma TP. *IEEE Electr Device Lett* 2002;**23**:649–51.
44. He Q, Guo H-B, Wei J-J, Askari SJ, Wang H-B, Zhang S-Y, Yang H, Su X-P, Lu F-X. *Thin Solid Films* 2008;**516**:4695–9.
45. Ferrari AC, Robertson J. *Phys Rev B* 2000;**61**:14095–107.
46. Tuinstra F, Koenig JL. *J Chem Phys* 1970;**53**:1126.
47. Thomsen C, Reich S. *Phys Rev Lett* 2000;**85**:5214–7.
48. Knight DS, White WB. *J Mater Res* 1988;**4**:385–93.
49. Brown SDM, Jorio A, Dresselhaus MS, Dresselhaus G. *Phys Rev B* 2001;**64**:073403.
50. Mariotto G, Vinegoni C, Jacobsohn LG, Freire Jr FL. *Diam Relat Mater* 1999;**8**:668–72.
51. Capelli E, Orlando S, Mattei G, Scilletta C, Corticelli F, Ascarelli P. *Appl Phys A* 2004;**79**:2063–8.
52. Casiraghi C, Piazza F, Ferrari AC, Grambole D, Robertson J. *Diam Relat Mater* 2005;**14**:1098–102.
53. errari AC, Robertson J. *Phys Rev B* 2001;**64**:075414.
54. Tkachev SN, Manghnani MH, Niilisk A, Aarik J, Mändar H. *Spectrochim Acta Part A* 2005;**61**:2434–8.
55. Temple PA, Hathaway CE. *Phys Rev B* 1973;**7**:3685–97.
56. Robertson J. *Phys Rev B* 1996;**53**:16302–5.
57. Conway NMJ, Ferrari AC, Flewitt AJ, Robertson J, Milne WI, Tagliaferro A, Beyer W. *Diam Relat Mater* 2000;**9**:765–70.
58. Ilie A, Ferrari AC, Yagi T, Robertson J. *Appl Phys Lett* 2000;**76**:2627–9.
59. Okabe H. *Can J Chem* 1983;**61**:850–5.
60. Tallant DR, Permeter JE, Siegal MP, Simpson RL. *Diam Relat Mater* 1995;**4**:191–9.